Published in final edited form as:

Nano Lett. 2023 February 08; 23(3): 969–978. doi:10.1021/acs.nanolett.2c04420.

High-Throughput DFT-Based Discovery of Next Generation Two-Dimensional (2D) Superconductors

Daniel Wines,
Material Measurement Laboratory, National Institute of Standards and Technology, Gaithersburg, Maryland 20899, United States

Kamal Choudhary,
Material Measurement Laboratory, National Institute of Standards and Technology, Gaithersburg, Maryland 20899, United States; Theiss Research, La Jolla, California 92037, United States

Adam J. Biacchi,
Physical Measurement Laboratory, National Institute of Standards and Technology, Gaithersburg, Maryland 20899, United States

Kevin F. Garrity,
Material Measurement Laboratory, National Institute of Standards and Technology, Gaithersburg, Maryland 20899, United States

Francesca Tavazza
Material Measurement Laboratory, National Institute of Standards and Technology, Gaithersburg, Maryland 20899, United States

Abstract

High-throughput density functional theory (DFT) calculations allow for a systematic search for conventional superconductors. With the recent interest in two-dimensional (2D) superconductors, we used a high-throughput workflow to screen over 1000 2D materials in the JARVIS-DFT database and performed electron–phonon coupling calculations, using the McMillan–Allen–Dynes formula to calculate the superconducting transition temperature (T_c) for 165 of them. Of these 165 materials, we identify 34 dynamically stable structures with transition temperatures above 5 K, including materials such as W_2N_3, NbO_2, ZrBrO, TiClO, $NaSn_2S_4$, $Mg_2B_4C_2$, and the previously unreported $Mg_2B_4N_2$ (T_c = 21.8 K). Finally, we performed experiments to determine the T_c of

Corresponding Author: Daniel Wines – daniel.wines@nist.gov.

The authors declare no competing financial interest.

Certain commercial equipment or materials are identified in this paper to adequately specify the experimental procedures. In no case does the identification imply recommendation or endorsement by NIST, nor does it imply that the materials or equipment identified are necessarily the best available for the purpose. Note that the use of commercial software (VASP) does not imply recommendation by the National Institute of Standards and Technology.

Code Availability Statement. Software packages mentioned in the article can be found at https://github.com/usnistgov/jarvis.

Complete contact information is available at: https://pubs.acs.org/10.1021/acs.nanolett.2c04420

ASSOCIATED CONTENT
Supporting Information
The Supporting Information is available free of charge at https://pubs.acs.org/doi/10.1021/acs.nanolett.2c04420.
Experimental methods, additional convergence details, additional details of data set, phonon density of states, and list of newly added structures to JARVIS (PDF)

selected layered superconductors (2H-$NbSe_2$, 2H-NbS_2, ZrSiS, FeSe) and discuss the measured results within the context of our DFT results. We aim that the outcome of this workflow can guide future computational and experimental studies of new and emerging 2D superconductors by providing a roadmap of high-throughput DFT data.

Graphical Abstract

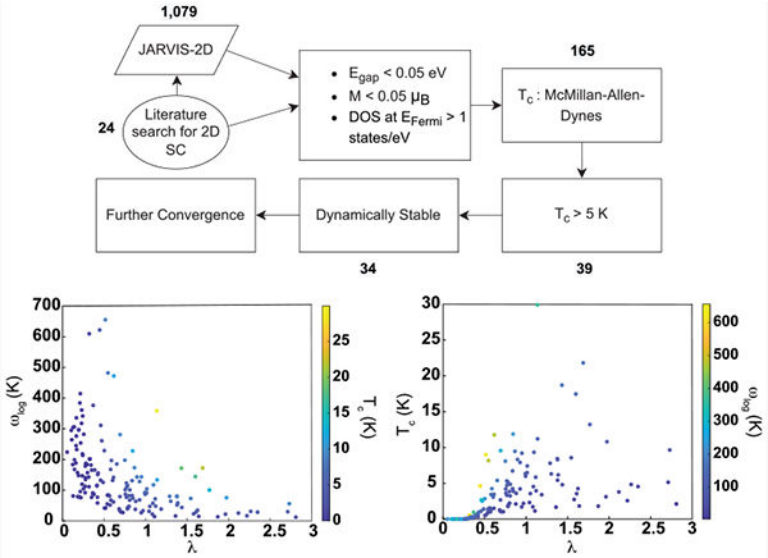

Keywords

2D superconductivity; density functional theory; high-throughput; materials discovery

In the past decade, superconductivity in two-dimensional (2D) systems has attracted a great deal of attention due to its potential applications for nanoscale devices such as superconducting transistors, quantum interferometers, and superconducting qubits.[1–5] Since the significant experimental work of Zhang et al. in 2010, which demonstrated superconductivity up to 1.8 K in single-layer Pb on Si(111),[6] the quest to synthesize and theoretically predict 2D superconducting materials has moved toward intrinsically 2D monolayers whose bulk counterparts are weakly bonded layered materials.[7–9] On the experimental front, a superconducting transition has been predicted for a variety of alkali-decorated graphene layers, with transitions reported for K-intercalated few-layer graphene at 4.5 K,[10] as well as for Li- and Ca-intercalated graphene.[11–13] In addition, superconductivity has been measured for a variety of few-layer and monolayer transition metal dichalcogenides (TMDs) with a critical temperature of 7.2 K for $NbSe_2$,[14–17] 5.3 K for NbS_2,[18,19] 3 K for $TiSe_2$,[20] 2.2 K for TaS_2,[21] and between 7 and 12 K for MoS_2.[22–25]

Using first-principles calculations, efforts have been made to screen 2D superconducting monolayers with higher T_c including intrinsic 2D metals and doped 2D materials.[26–30] Two dimensional boron allotropes (such as borophene)[31–35] and carbon–boron based 2D materials such as B_2O,[36] B_2C,[37] LiBC,[38] MgB_2,[39] Mo_2C,[40] $Mg_2B_4C_2$,[41] and W_2N_3[42] have been predicted to have substantial critical temperatures. Specifically, $Mg_2B_4C_2$ and

W_2N_3 have been predicted to have a T_c of 47 and 21 K, respectively.[41,42] Computational predictions of superconducting transition temperatures can be most useful as a precursor to direct more expensive and time-consuming experimental synthesis and characterization. Previously, there have been several efforts to systematically discover superconducting materials which fall into certain materials classes, such as transition metals,[43] A15, B1,[44,45] AB_2 compounds,[46–48] cuprates,[49] iron-based compounds,[50] hydrides,[51–53] and many other classes of materials.[48,54–62]

To efficiently identify Bardeen–Cooper–Schrieffer (BCS) conventional superconductors[63,64] with high critical temperatures using computational methods, there are two main requirements: (1) a robust computational workflow and (2) a curated database of materials with prior knowledge such as band structure, magnetic properties, and electronic density of states. Using density functional theory perturbation theory (DFT-PT), the electron–phonon coupling (EPC) can be calculated and used to predict T_c with reasonable accuracy for a variety of materials.[64,65] In this work, we designed a systematic, data-driven workflow to expedite the discovery of new and potentially high-T_c 2D superconductors. We do so by combining several computational methods at various levels of cost and accuracy. We start with a BCS-inspired prescreening for metallic, nonmagnetic materials with high electron density of states (DOS) at the Fermi level ($N(0)$), using the existing Joint Automated Repository for Various Integrated Simulations (JARVIS) DFT database for 2D materials.[66] Additionally, we searched existing literature for 2D superconductors not already in the JARVIS-DFT database and added them as appropriate. We then applied our DFT-PT workflow to compute T_c using the EPC and the McMillan–Allen–Dynes formula,[67] with low convergence settings initially (k-points, q-points). For the most ideal candidates, we performed additional convergence to increase the accuracy of our predictions.

A key component in achieving an efficient search for 2D superconducting materials was to utilize the JARVIS (https://jarvis.nist.gov/)[66] infrastructure, which is a collection of databases and tools to automate materials design using density functional theory, classical force-fields, machine learning, and experiments. JARVIS-DFT is a density functional theory based database of over 60 000 bulk materials and over 1000 2D and 2D-like materials. Material properties are formation energy, band gap,[68] exfoliation energies,[69] solar-cell efficiency,[70] spin–orbit spillage,[71–73] elastic tensors,[74] dielectric tensors, piezoelectric tensors, infrared and Raman spectra,[75] electric field gradients,[76] accurate magnetic properties,[77] and superconducting transition temperature of bulk materials,[78] all with strict and careful DFT-convergence criteria.[79]

BCS-theory[80] states that the attractive electron–electron interaction mediated by phonons results in Cooper pairs, which are bound states that are formed by two electrons with opposite spins and momenta. BCS theory gives the relation between the Debye temperature (θ_D), electronic DOS at Fermi level $N(0)$, electron–phonon interaction (V), and the superconducting transition temperature (T_c):

$$T_c = 1.14\theta_D \exp\left(-\frac{1}{N(0)V}\right) \quad (1)$$

θ_D is defined as[81]

$$\theta_D = \frac{h}{k_B}\left[\frac{3nN_A\rho}{4\pi M}\right]^{1/3} v_m \quad (2)$$

where h is Planck's constant, k_B is the Boltzmann constant, n is the number of atoms per formula unit, N_A is Avogadro constant, ρ is the crystal structure's density, M is the molar mass, and v_m is the average sound velocity obtained from the elastic tensor.[81]

In our previous work on bulk materials,[78] we used the θ_D obtained from finite-difference calculations of elastic tensors[74] (JARVIS-DFT contains elastic tensors for over 17 000 bulk materials). However, because of the lack of periodicity in one direction for 2D materials, the calculation of the elastic constants requires more careful consideration (performing several calculations of biaxial strain and then polynomial fitting, to allow for buckling in the out-of-plane direction). For this reason, elastic constants have not been computed for the over 1000 2D materials in JARVIS-DFT. As a result, we cannot use θ_D as a screening metric. Instead, we must independently consider $N(0)$ in eq 1 and screen based on the fact that a large $N(0)$ will yield a large value for T_c. This limitation to the screening is compensated by adding additional screening metrics such as band gap and magnetic moment to the criteria. Instead, our initial screening is based on $N(0)$, the DOS at the Fermi level, which is available in JARVIS-DFT. We additionally screened materials based on whether or not they were nonmagnetic and added candidate 2D superconducting materials to the JARVIS-DFT database from searching the literature.

The JARVIS-DFT database is primarily populated by calculations made using the Vienna ab initio simulation package (VASP)[82,83] software and the OptB88vdW[84] functional. The k-points are carefully converged in JARVIS-DFT with respect to total energy.[79] We used these converged k-points in subsequent Quantum Espresso[85,86] electron–phonon calculations.

The properties of conventional BCS superconductors are directly related to the EPC. EPC calculations can be performed by methods such as the interpolated/Gaussian broadening method,[87] tetrahedron method,[88] and Wannier-based electron–phonon methods.[89] In the interpolated method, the integration over k-points involves replacing the δ function with a smeared function which has a finite broadening width, where the broadening width must be converged to obtain accurate results.[87] In the tetrahedron method, the k-points are analytically integrated in tetrahedral regions covering the Brillouin zone with the piecewise linear interpolation of a matrix element.[88] Similar to the justification of our previous work,[78] we used the interpolated method for the EPC calculations due to the fact that our results obtained with the interpolation method are computationally less expensive and more stable (less variability with respect to k- and q-points) than the tetrahedron method. Since the interpolated method was used, the value for broadening was carefully converged for each material.

We performed the EPC calculations using DFT-PT[90,91] with the Quantum Espresso code,[85] the Perdew–Burke–Ernzerhof functional revised for solids (PBEsol),[92] and Garrity–Bennett–Rabe–Vanderbilt (GBRV)[93] pseudopotentials. The starting structures were from the JARVIS-DFT 2D database (relaxed with OptB88vdW), and we performed a full rerelaxation

with Quantum Espresso. In the Quantum Espresso rerelaxation, the unit cell and atomic positions were allowed to relax to minimize the force and external pressure on the system. The energy convergence value between two consecutive steps was chosen to be 10×10^{-8} eV, and a maximum pressure of 0.5 kbar was allowed on the cell. After rerelaxing the structures with Quantum Espresso (using PBEsol and GBRV potentials), we obtained similar results to the original structure from JARVIS relaxed with VASP using OptB88vdW (i.e., there was about an average ≈1–2% difference in in-plane lattice constant between the two methods). Similar to our previous work,[78] we used a 610 eV (45 Ry) plane-wave cutoff since we find that higher values have minimal effect on the calculated EPC parameters. The EPC parameter is derived from spectral function $\alpha^2F(\omega)$, which is given by

$$\alpha^2F(\omega) = \frac{1}{2\pi N(\epsilon_F)} \sum_{qj} \frac{\gamma_{qj}}{\omega_{qj}} \delta(\omega - \omega_{qj}) w(q) \tag{3}$$

where ω_{qj} is the mode frequency, $N(\epsilon_F)$ is the DOS at the Fermi level ϵ_F, δ is the Dirac δ function, $w(q)$ is the weight of the q point, and γ_{qj} is the line width of a phonon mode j at wave vector q and can be written as

$$\gamma_{qj} = 2\pi\omega_{qj} \sum_{nm} \int \frac{d^3k}{\Omega_{BZ}} |g^j_{kn,\,k+qm}|^2 \delta(\epsilon_{kn} - \epsilon_F) \delta(\epsilon_{k+qm} - \epsilon_F) \tag{4}$$

In this equation, the integral is over the first Brillouin zone, ϵ_{kn} and ϵ_{k+qm} are the eigenvalues from DFT with wavevector k and $k + q$ within the nth and mth bands, respectively, and $g^j_{kn,\,k+qm}$ is the electron–phonon matrix element. The relation between γ_{qj} and the mode EPC parameter λ_{qj} is as follows:

$$\lambda_{qj} = \frac{\gamma_{qj}}{\pi h N(\epsilon_F) \omega^2_{qj}} \tag{5}$$

The EPC parameter is now given by

$$\lambda = 2 \int \frac{\alpha^2F(\omega)}{\omega} d\omega = \sum_{qj} \lambda_{qj} w(q) \tag{6}$$

with $w(q)$ as the weight of a q point.

The superconducting transition temperature, T_c can be approximated by using the original McMillan–Allen–Dynes[67] equation:

$$T_c = \frac{\omega_{log}}{1.2} \exp\left[-\frac{1.04(1 + \lambda)}{\lambda - \mu^*(1 + 0.62\lambda)}\right] \tag{7}$$

where

$$\omega_{\log} = \exp\left[\frac{\int \mathrm{d}\omega \frac{\alpha^2 F(\omega)}{\omega} \ln \omega}{\int \mathrm{d}\omega \frac{\alpha^2 F(\omega)}{\omega}}\right] \quad (8)$$

In eq 7, the μ^* parameter is the effective Coulomb potential. Although this parameter can be calculated from first principles,[94] μ^* generally varies over a relatively small range (such as 0.09–0.18). Similar to several other studies involving 2D materials,[36,37,41] we take $\mu^* = 0.1$ when reporting our results from high-throughput screening.

A full schematic of the high-throughput workflow we used to identify 2D superconductors with high T_c is shown in Figure 1. The starting point involves the screening of properties of the 1079 monolayer materials to date in the JARVIS-DFT database. These 1079 materials span a wide range of chemical and structural space, and their inclusion in the JARVIS-DFT database stems from studies involving high-throughput identification and characterization of 2D materials,[69] investigation of elastic properties of 2D materials,[74] the discovery of 2D solar cell materials,[70] discovery and characterization of 2D heterostructures,[95] and the high-throughput search for 2D topological materials,[73] thermoelectric materials,[96] and anomalous quantum confinement materials.[97] Due to the fact that the elastic tensor (and therefore the Debye temperature) is more computationally expensive to compute for 2D materials than bulk materials, it is only available for a selected number of 2D materials in the JARVIS-DFT database. For this reason, we had to modify the BCS screening workflow that was used in our previous work.[78] Instead of screening the density of states (DOS) at the Fermi level and the Debye temperature (as we did for bulk materials), we screened materials based on the density of states (DOS) at the Fermi level, the total magnetic moment, and the electronic band gap (calculated with the OptB88vdW functional). This screening process is based on the notion that a potential 2D superconductor will have a high density of states at the Fermi level (and therefore be metallic), which is inspired by the BCS equation for T_c (see eq 1). In addition, for simplicity, we selected structures with zero magnetic moment per unit cell to avoid the magnetic moment interfering with the EPC. The EPC calculations carried out based on this screening are non-spin-polarized. Based on this, we established a quantitative criteria for 2D superconductor screening depicted in Figure 1.

In addition to selecting 2D materials in JARVIS that meet the criteria of $E_{gap} < 0.05$ eV, $M < 0.05\ \mu_B$, and DOS at $E_{Fermi} > 1$ states/eV/Nelect, we identified 24 additional 2D materials, based on an extensive literature search of 2D and 3D superconductors. These 24 2D materials were added to JARVIS-DFT and include $Mg_2B_4N_2$, W_2N_3, MgB_2, Mo_2C, B_2N, $Mg_2B_4C_2$, χ and β phase borophene, ZrSiS, NbC, α-$Mg_2B_4N_2$, B_2O, 2H-$NbTe_2$, 1T-$NbTe_2$, 2H-$TaTe_2$, 1T-$TaTe_2$, LiC_6, CaC_6, $PdBi_2$, W_2B_3, MgBH, ScC, Al_4CO, and $CaRu_2N_2$. Although several of these 2D materials have been studied with ab initio methods in previous works, to our knowledge, this is the first reported instance of 2D W_2B_3, $Mg_2B_4N_2$ (both phases), MgBH, NbC, ScC, and $CaRu_2N_2$.

In order to fully converge the EPC calculations with DFT-PT, a significant amount of computational resources are needed. These calculations generally require a dense k-point grid to sample electronic states and a dense q-point grid to sample phonons.[87] This becomes

increasingly difficult for larger unit cells since the number of modes needed for calculation at each q-point increases as the number of atoms in the cell increases. In the Supporting Information, we display a number of convergence checks needed to determine the minimal set of parameters necessary to obtain a converged estimate of T_c. The quantities of interest include the number of k-points for the self-consistent DFT calculation, the number of q-points for the DFT-PT calculation, the broadening value used for the linear interpolation, and the value for μ^* (in eq 7). In our previous work, we extensively investigated the effects of these parameters on the converged results.[78]

We adopt a similar, less extensive procedure for selected 2D materials to confirm that our convergence criteria for bulk materials is valid in the 2D case. In Figure S1 we show the convergence of λ, ω_{log}, and T_c with respect to different k-point and q-point grids with respect to broadening for the 2H-$NbSe_2$ compound, which is a well-known 2D superconductor experimentally with a high T_c value. From Figure S1a–c, we observe that as the q-point grid increases, the T_c value has less of a dependence on the k-point grid. From analyzing all combinations of k-point and q-point grids, we calculate T_c values that range from 4.5 to 7.6 K. This is within reasonable agreement with respect to the experimental value of 7.2 K from literature,[14–17] and we believe it is an acceptable margin of error for the high-throughput DFT–Allen–McMillan-Dynes method to obtain T_c. We also observe that a broadening parameter of 0.68 eV (0.05 Ry) is sufficient in converging the T_c result within our desired tolerance, similar to our previous work.[78] This behavior is similar to the additional convergence tests we performed on a selected group of monolayers ($Mg_2B_4N_2$, W_2N_3, TiClO, NbO_2, 2H-NbS_2, ZrBrO, 2H-$NbSe_2$) shown in Figure S2, which all display a converged T_c value with respect to a broadening value of 0.68 eV (0.05 Ry). Additional q-point convergence (using the converged k-grid from JARVIS-DFT) for data is presented in Table S1 for 2D 2H-TaS_2, 2H-$NbSe_2$, W_2N_3, $Mg_2B_4N_2$, and TiClO. Based on these results, we determined that q-point grids as small as $2 \times 2 \times 1$ combined with k-point grids similar in size to the typical grids used for self-consistent DFT total energy calculations (k-point grid obtained from JARVIS-DFT total energy convergence[79]) are sufficient to identify candidate 2D superconducting materials, along with a broadening of 0.68 eV (0.05 Ry). For selected promising candidate materials for which it was computationally feasible, we ran additional calculations with higher convergence parameters (see Table S2, which is an extension of Table 1 to include the k-point and q-point grids used in the calculation).

In addition to the k-point, q-point and broadening convergence, we also addressed the impact of μ^* in our calculations.[64,87,94,98] As previously mentioned, μ^* is the effective Coulomb potential in eq 7. Since it is computationally expensive to calculate this parameter from first principles, it is usually used as a fitting parameter for the calculation of T_c and commonly taken as $\mu^* = 0.1$. In Figure S2d, we plot the value of T_c calculated with varying values of μ^*, ranging from 0.03 to 0.22 for a selected group of representative superconductors ($Mg_2B_4N_2$, W_2N_3, TiClO, NbO_2, 2H-NbS_2, ZrBrO). We observe a remarkably consistent trend between all of these materials, with the T_c values varying linearly with respect to the change in μ^*. Across all six of these materials, we observe similar slopes (see Figure S2d), with the slight exception of TiClO which has a smaller slope compared to the other materials due to the fact that it has a much larger value for λ and a much smaller value for ω_{log}. It is important to note that these six materials retain their

superconducting properties despite a large range of μ^* values. The loss of superconducting properties at large values of μ^* has been reported for a large variety of bulk materials.[78] For the sake of being concise and consistent with previous works,[42] we report T_c values calculated with $\mu^* = 0.1$.

We applied our high-throughput screening technique to the 1079 monolayers in the JARVIS-DFT database. From this set of materials and the 24 monolayers we added from literature, we found 165 materials that fit our criteria to perform the DFT-PT and McMillan–Allen–Dynes EPC calculation for. Similar to our previous work,[78] we ignore spin–orbit coupling, spin-polarization, Hubbard (+U) correction,[99] and spin-fluctuation[100,101] contributions due to the higher computational cost of such calculations. For a more accurate description of the underlying physics of these 2D superconductors, these effects should be considered in follow-up work. Of the 165 2D materials that we ran the EPC workflow for, we find that 34 have a T_c greater than 5 K and are dynamically stable (no imaginary phonon modes), which is an extremely promising result. It is also important to note that 11 of the 24 compounds that were added to JARVIS based on a literature search fit the criteria of a T_c greater than 5 K and dynamic stability (included in the 34).

The tabulated results for these 34 materials are given in Table 1, where the chemical formula and EPC results are provided for each material (λ, ω_{log}, T_c), together with their OptB88vdW-based formation energy per atom (E_{form}) from JARVIS-DFT. Out of these 34 materials, we ran the EPC calculation with the highest convergence parameters that were computationally tractable (k-point, q-point). The k-point and q-point grids used in the EPC calculations are given in Table S2. The JARVIS IDs of each material (including the 24 newly added monolayers to JARVIS-DFT) are given in Table 1 and Table S2.

We find that several candidate 2D superconductors that have a T_c above 5 K are based on nitrides, borides, and carbides (see Table 1). In addition, several oxide and niobium-based compounds and transition metal dichalcogenides such as NbS_2/Se_2 in both their 2H (two "layers" per hexagonal unit cell) and 1T (one layer per trigonal unit cell) phases exhibit strong superconducting properties. Remarkably, 26 of these 34 materials have a formation energy less than or equal to 0.10 eV/atom and 23 of those 26 materials have negative formation energy, which signifies the likelihood that these materials can be synthesized and be stable in monolayer form. To further quantify this, we depict the phonon density of states for a selected number of structures with positive formation energy (see Figure S3), where we see that although formation energy is positive, these structures are dynamically stable. In Figure 2, we depict the geometric structure of several of the promising candidate 2D superconductors for experimental synthesis. The JARVIS ID of each material (which can be obtained from Table 1 and Table S2) can be used to obtain further properties and details.

We observe the highest transition temperature for monolayer $Mg_2B_4N_2$, which has a T_c of 21.8 K. To our knowledge, this material has previously been undiscovered in bulk and 2D form. The motivation to study $Mg_2B_4N_2$ stems from the recent prediction of a high superconducting temperature (47 K)[41] for $Mg_2B_4C_2$. In our work, we calculated the T_c of 2D $Mg_2B_4C_2$ to be 9.0 K. The difference between the T_c obtained in our work versus previous work can be attributed to the differences in calculation methods used

(different codes, pseudopotentials, density functionals, method of perturbation theory/EPC calculation[41]). Nevertheless, the substitution of carbon with nitrogen results in over a 155% increase in the superconducting transition temperature. Qualitatively this is an extremely promising result, and because it has negative formation energy, there is a strong motivation for experimentalists to pursue 2D $Mg_2B_4N_2$. Although we observe promising EPC properties for the $Mg_2B_4N_2$ monolayer, we observe that the B–N layers get slightly separated from the Mg–B after atomic relaxation. The atomic projected density of states indicates that contribution of s and p states of Mg and p states of B is greatest around the Fermi level, while the atomic contribution of the B–N layers is away from the Fermi level. This implies that it is possible that there exists a hole-rich inner Mg–B slab in between two saturated B–N layers, where the EPC properties (high T_c) is coming mostly from the inner Mg–B layer. In addition, we found another previously unknown layered polymorph of $Mg_2B_4N_2$ (which we deem α-$Mg_2B_4N_2$) with a high T_c of 7.4 K. This hypothetical polymorph has a higher formation energy than the other $Mg_2B_4N_2$ structure (0.06 eV/atom vs −0.24 eV/atom). Consistent with recent EPC calculations,[42] we find W_2N_3 to have a notably high T_c of 18.7 K. Motivated by the investigation of $Mg_2B_4N_2$, we decided to substitute N with B in W_2N_3. We find a significant decrease in superconducting properties of the previously undiscovered W_2B_3 (JVASP-153120), with a calculated T_c of 1.0 K. Our results on $Mg_2B_4C_2/N_2$ and W_2N_3/B_3 demonstrate how direct substitution can effectively tune the superconducting properties of a 2D material, which can be explored further in future work. We also investigated several 2D analogs of nonlayered boron, carbon, and nitrogen-based materials bulk materials (such as 2D MgB_2, B_2N, NbC, ScC, etc.). Although several of these monolayers have a high T_c value (see Table 1), they have significantly positive formation energy, which makes their experimental realization less likely. In contrast, several 2D oxide-based materials (NbO_2, ZrBrO, TiClO, etc.) possess negative formation energy and strong superconducting properties.

In Figure 3a,b, we show the relationship between EPC parameters for all of the considered 2D materials in this study. In Figure 3a we observe that λ and ω_{log} have an inverse relationship, and in Figure 3b, we observe a positive relationship between λ and T_c. Both of these behaviors are typical of BCS superconductors and were already observed in our work on BCS bulk superconductors.[78] As evident from the colormap of Figure 3a,b, a balance of high λ and ω_{log} is necessary for a material to have a high T_c. In Figure 3c–e, we depict a few examples of the Eliashberg spectral functions of some of the candidate materials (W_2N_3, $Mg_2B_4C_2$, and 2H-$NbSe_2$). The Eliashberg spectral function expresses the electron–phonon interaction in the form of a spectral density, and the weighted area underneath the EPC function determines the λ and ω_{log} parameters. These Eliashberg spectral functions and EPC parameters, along with several other material properties, can be obtained from the JARVIS-DFT database.

In order to gain a deeper understanding of some of the materials we considered in this study, we performed zero field-cooled magnetometry experiments to determine the critical temperature. These measurements were done on powder samples, with the intention that they will be representative of the inherent 2D layered structure (although the discrepancy between single layer and bulk layered form is larger for certain materials). We conducted these experiments for layered 2H-$NbSe_2$, 2H-NbS_2, FeSe, and ZrSiS. Similar measurements

have been conducted for 2H-$NbSe_2$, 2H-NbS_2, and FeSe, but to our knowledge, they have not been conducted for layered ZrSiS. Unfortunately, we could not conduct these zero field-cooled magnetometry experiments on some of the high T_c materials such as W_2N_3, $Mg_2B_4N_2$, $Mg_2B_4C_2$, and several others due to the fact that they are not yet commercially available. Figure 4 depicts the measured magnetic susceptibility (using a magnetic field strength of 0.01 T) as a function of temperature. We observe that out of these layered materials, 2H-$NbSe_2$ has a T_c of 8.3 K, 2H-NbS_2 has a T_c of 7.1 K, FeSe has a T_c of 7.5 K, and ZrSiS does not have a superconducting transition due to the decreasing magnetic susceptibility with increasing temperature. The experimental results for layered 2H-$NbSe_2$ and 2H-NbS_2 are in excellent agreement (within ≈2 K) of the results we calculated for monolayer 2H-$NbSe_2$ and 2H-NbS_2 (see Table 1). Interestingly, layered ZrSiS (known to be a Dirac semimetal with topological properties[102,103]) does not possess superconducting properties, while our calculations for monolayer ZrSiS result in a high value of T_c (7.9 K). The reason for this discrepancy stems from the major differences in the properties of the bulk layered structure vs monolayer ZrSiS. In our previous work,[78] we calculated a T_c of zero for bulk ZrSiS (JVASP-15288), which is consistent with the current measurements in Figure 4d. The presence of superconductivity in the monolayer and absence of superconductivity in the bulk structure are also consistent with previous experimental literature, where tip-induced superconductivity (with a T_c of 7.5 K) was observed in single crystal ZrSiS.[103] This can also be due in part to the fact that bulk ZrSiS has a smaller interlayer [vertical distance between consecutive layers in the bulk layered material, as opposed to the out of plane lattice constant *c*] distance (JVASP-15288, 2.2 Å) compared to the interlayer distances of bulk NbS_2 (JVASP-30369, 3.4 Å), $NbSe_2$ (JVASP-31795, 3.1 Å), and FeSe (JVASP-45, 2.8 Å).

Finally, we decided to study layered FeSe due to the large amount of attention it has received in the past decade after superconductivity above 100 K was measured in single-layer FeSe films on a doped $SrTiO_3$ substrate.[104] Although we measure a high T_c of 7.5 K for layered FeSe, we calculated a T_c of 1.0 K for monolayer FeSe (JVASP-60244, the low T_c is why it is absent from Table 1). We went on to calculate the EPC properties of bulk layered FeSe (JVASP-45) for comparison, and we find that it does not have a superconducting critical temperature (consistent with previous nonmagnetic DFT results for layered FeSe [105]). The qualitative comparison between monolayer and bulk FeSe is significant in showing how the superconducting properties can be enhanced from the bulk to monolayer limit. The discrepancy between experiment and theory can be due in part to spin polarization not being taken into account. This is emphasized by previous computational studies where a substantial T_c value was calculated for the antiferromagnetic orientation of FeSe.[106] These magnetic interactions of certain layered superconductors can play an important role in the calculation of accurate EPC parameters, but such calculations are beyond the scope of this high-throughput work and may be considered in future studies.

In summary, we have used a high-throughput DFT approach to study conventional 2D BCS superconductors, finding 34 candidate materials with a predicted T_c above 5 K. Due to our high-throughput approach, we employ several approximations and assumptions, but we perform significant benchmarking tests and convergence checks on particular materials to verify our results and methodology. We went one step further and performed experiments

on selected layered superconductors to obtain the measured critical temperature. Our tools and data sets are publicly available (as a part of the JARVIS-DFT database) to enhance the transparency and reproducibility of this ongoing work. Possible applications of these additions to the JARVIS database include the data being used for training of various machine learning and generative models that can aid in the discovery of new superconductors. The calculated data can also be used for screening purposes for researchers who wish to tune the properties of promising 2D superconductors with methods such as applying pressure, alloying, or creating heterostructures. We believe the results of this study can guide future computational and experimental studies of new and emerging 2D superconductors by providing a roadmap of high-throughput DFT data.

Supplementary Material

Refer to Web version on PubMed Central for supplementary material.

ACKNOWLEDGMENTS

All authors thank the National Institute of Standards and Technology for funding, computational, and data-management resources. K.C. thanks the computational support from XSEDE (Extreme Science and Engineering Discovery Environment) computational resources under Allocation TG-DMR 190095. Contributions from K.C. were supported by Financial Assistance Award 70NANB19H117 from the U.S. Department of Commerce, National Institute of Standards and Technology. The authors thank Dr. Sobhit Singh for helpful discussions during the preparation of this manuscript.

Data Availability Statement

The data from the present work can be found at https://figshare.com/articles/dataset/JARVIS-SuperconDB/21370572.

REFERENCES

(1). De Franceschi S; Kouwenhoven L; Schönenberger C; Wernsdorfer W Hybrid superconductor-quantum dot devices. Nat. Nanotechnol. 2010, 5, 703–711. [PubMed: 20852639]

(2). Huefner M; May C; Kicin S; Ensslin K; Ihn T; Hilke M; Suter K; de Rooij NF; Staufer U Scanning gate microscopy measurements on a superconducting single-electron transistor. Phys. Rev. B 2009, 79, 134530.

(3). Delahaye J; Hassel J; Lindell R; Sillanpää M; Paalanen M; Seppä H; Hakonen P Low-Noise Current Amplifier Based on Mesoscopic Josephson Junction. Science 2003, 299, 1045–1048. [PubMed: 12586938]

(4). Romans EJ; Osley EJ; Young L; Warburton PA; Li W Three-dimensional nanoscale superconducting quantum interference device pickup loops. Appl. Phys. Lett. 2010, 97, 222506.

(5). Liu X; Hersam MC 2D materials for quantum information science. Nature Reviews Materials 2019, 4, 669–684.

(6). Zhang T; Cheng P; Li W-J; Sun Y-J; Wang G; Zhu X-G; He K; Wang L; Ma X; Chen X; Wang Y; Liu Y; Lin H-Q; Jia J-F; Xue Q-K Superconductivity in one-atomic-layer metal films grown on Si(111). Nat. Phys. 2010, 6, 104–108.

(7). Saito Y; Nojima T; Iwasa Y Highly crystalline 2D superconductors. Nat. Rev. Mater. 2017, 2, 16094.

(8). Brun C; Cren T; Roditchev D Review of 2D superconductivity: the ultimate case of epitaxial monolayers. Supercond. Sci. Technol. 2017, 30, 013003.

(9). Saito Y; Nojima T; Iwasa Y Gate-induced superconductivity in two-dimensional atomic crystals. Supercond. Sci. Technol. 2016, 29, 093001.

(10). Xue M; Chen G; Yang H; Zhu Y; Wang D; He J; Cao T Superconductivity in Potassium-Doped Few-Layer Graphene. J. Am. Chem. Soc. 2012, 134, 6536–6539. [PubMed: 22471507]

(11). Tiwari AP; Shin S; Hwang E; Jung S-G; Park T; Lee H Superconductivity at 7.4 K in few layer graphene by Li-intercalation. J. Phys.: Condens. Matter 2017, 29, 445701. [PubMed: 28850047]

(12). Ludbrook BM; et al. Evidence for superconductivity in Li-decorated monolayer graphene. Proc. Natl. Acad. Sci. U. S. A. 2015, 112, 11795–11799. [PubMed: 26351697]

(13). Li K; Feng X; Zhang W; Ou Y; Chen L; He K; Wang L-L; Guo L; Liu G; Xue Q-K; Ma X Superconductivity in Ca-intercalated epitaxial graphene on silicon carbide. Appl. Phys. Lett. 2013, 103, 062601.

(14). Frindt RF Superconductivity in Ultrathin $NbSe_2$ Layers. Phys. Rev. Lett. 1972, 28, 299–301.

(15). Ugeda MM; et al. Characterization of collective ground states in single-layer NbSe2. Nat. Phys. 2016, 12, 92–97.

(16). Tsen AW; Hunt B; Kim YD; Yuan ZJ; Jia S; Cava RJ; Hone J; Kim P; Dean CR; Pasupathy AN Nature of the quantum metal in a two-dimensional crystalline superconductor. Nat. Phys. 2016, 12, 208–212.

(17). Xi X; Wang Z; Zhao W; Park J-H; Law KT; Berger H; Forró L; Shan J; Mak KF Ising pairing in superconducting NbSe2 atomic layers. Nat. Phys. 2016, 12, 139–143.

(18). Guillamón I; Suderow H; Vieira S; Cario L; Diener P; Rodière P Superconducting Density of States and Vortex Cores of 2H-NbS_2. Phys. Rev. Lett. 2008, 101, 166407. [PubMed: 18999695]

(19). Yan R; Khalsa G; Schaefer BT; Jarjour A; Rouvimov S; Nowack KC; Xing HG; Jena D Thickness dependence of superconductivity in ultrathin NbS_2. Applied Physics Express 2019, 12, 023008.

(20). Li LJ; O'Farrell ECT; Loh KP; Eda G; Özyilmaz B; Castro Neto AH Controlling many-body states by the electric-field effect in a two-dimensional material. Nature 2016, 529, 185–189. [PubMed: 26700810]

(21). Navarro-Moratalla E; Island JO; Manas-Valero S; Pinilla-Cienfuegos E; Castellanos-Gomez A; Quereda J; Rubio-Bollinger G; Chirolli L; Silva-Guillen JA; Agrait N; Steele GA; Guinea F; van der Zant HSJ; Coronado E Enhanced superconductivity in atomically thin TaS2. Nat. Commun. 2016, 7, 11043. [PubMed: 26984768]

(22). Lu JM; Zheliuk O; Leermakers I; Yuan NFQ; Zeitler U; Law KT; Ye JT Evidence for two-dimensional Ising superconductivity in gated MoS_2. Science 2015, 350, 1353–1357. [PubMed: 26563134]

(23). Ye JT; Zhang YJ; Akashi R; Bahramy MS; Arita R; Iwasa Y Superconducting Dome in a Gate-Tuned Band Insulator. Science 2012, 338, 1193–1196. [PubMed: 23197529]

(24). Fu Y; et al. Gated tuned superconductivity and phonon softening in monolayer and bilayer MoS2. npj Quantum Mater 2017, 2, 52.

(25). Costanzo D; Jo S; Berger H; Morpurgo AF Gate-induced superconductivity in atomically thin MoS2 crystals. Nat. Nanotechnol. 2016, 11, 339–344. [PubMed: 26751171]

(26). Shao DF; Lu WJ; Lv HY; Sun YP Electron-doped phosphorene: A potential monolayer superconductor. EPL (Europhysics Letters) 2014, 108, 67004.

(27). Huang GQ; Xing ZW; Xing DY Prediction of superconductivity in Li-intercalated bilayer phosphorene. Appl. Phys. Lett. 2015, 106, 113107.

(28). Huang GQ; Xing ZW; Xing DY Dynamical stability and superconductivity of Li-intercalated bilayer MoS_2: A first-principles prediction. Phys. Rev. B 2016, 93, 104511.

(29). Lugovskoi AV; Katsnelson MI; Rudenko AN Electron-phonon properties, structural stability, and superconductivity of doped antimonene. Phys. Rev. B 2019, 99, 064513.

(30). Zhang X; Zhou Y; Cui B; Zhao M; Liu F Theoretical Discovery of a Superconducting Two-Dimensional Metal-Organic Framework. Nano Lett. 2017, 17, 6166–6170. [PubMed: 28898086]

(31). Gao M; Li Q-Z; Yan X-W; Wang J Prediction of phonon-mediated superconductivity in borophene. Phys. Rev. B 2017, 95, 024505.

(32). Penev ES; Kutana A; Yakobson BI Can Two-Dimensional Boron Superconduct? Nano Lett. 2016, 16, 2522–2526. [PubMed: 27003635]

(33). Mannix AJ; Zhou X-F; Kiraly B; Wood JD; Alducin D; Myers BD; Liu X; Fisher BL; Santiago U; Guest JR; Yacaman MJ; Ponce A; Oganov AR; Hersam MC; Guisinger NP Synthesis of borophenes: Anisotropic, two-dimensional boron polymorphs. Science 2015, 350, 1513–1516. [PubMed: 26680195]

(34). Xiao RC; Shao DF; Lu WJ; Lv HY; Li JY; Sun YP Enhanced superconductivity by strain and carrier-doping in borophene: A first principles prediction. Appl. Phys. Lett. 2016, 109, 122604.

(35). Feng B; Zhang J; Zhong Q; Li W; Li S; Li H; Cheng P; Meng S; Chen L; Wu K Experimental realization of two-dimensional boron sheets. Nat. Chem. 2016, 8, 563–568. [PubMed: 27219700]

(36). Yan L; Liu P-F; Li H; Tang Y; He J; Huang X; Wang B-T; Zhou L Theoretical dissection of superconductivity in two-dimensional honeycomb borophene oxide B2O crystal with a high stability. npj Comput. Mater. 2020, 6, 94.

(37). Dai J; Li Z; Yang J; Hou J A first-principles prediction of two-dimensional superconductivity in pristine B2C single layers. Nanoscale 2012, 4, 3032–3035. [PubMed: 22481534]

(38). Modak P; Verma AK; Mishra AK Prediction of superconductivity at 70 K in a pristine monolayer of LiBC. Phys. Rev. B 2021, 104, 054504.

(39). Bekaert J; Aperis A; Partoens B; Oppeneer PM; Milošević MV Evolution of multigap superconductivity in the atomically thin limit: Strain-enhanced three-gap superconductivity in monolayer MgB_2. Phys. Rev. B 2017, 96, 094510.

(40). Lei J; Kutana A; Yakobson BI Predicting stable phase monolayer Mo2C (MXene), a superconductor with chemically-tunable critical temperature. J. Mater. Chem. C 2017, 5, 3438–3444.

(41). Singh S; Romero AH; Mella J; Eremeev V; Muñoz E; Alexandrova AN; Rabe KM; Vanderbilt D; Muñoz F. High-temperature phonon-mediated superconductivity in monolayer Mg2B4C2. npj Quantum Mater. 2022, 7, 37.

(42). Campi D; Kumari S; Marzari N Prediction of Phonon-Mediated Superconductivity with High Critical Temperature in the Two-Dimensional Topological Semimetal W2N3. Nano Lett. 2021, 21, 3435–3442. [PubMed: 33856216]

(43). Roberts BW Survey of superconductive materials and critical evaluation of selected properties. J. Phys. Chem. Ref. Data 1976, 5, 581–822.

(44). Kihlstrom K; Simon R; Wolf S Tunneling α2F (ω) on high Tc A15 and B1 compounds. Physica B+C 1985, 135, 198–202.

(45). Stewart GR Superconductivity in the A15 structure. Physica C: Superconductivity and its Applications 2015, 514, 28–35.

(46). Ivanovskii A Band structure and properties of superconducting MgB2 and related compounds (a review). Phys. Solid State 2003, 45, 1829–1859.

(47). Buzea C; Yamashita T Review of the superconducting properties of MgB2. Supercond. Sci. Technol. 2001, 14, R115.

(48). Nagamatsu J; Nakagawa N; Muranaka T; Zenitani Y; Akimitsu J Superconductivity at 39 K in magnesium diboride. nature 2001, 410, 63–64. [PubMed: 11242039]

(49). Plakida N High-Temperature Cuprate Superconductors: Experiment, Theory, and Applications; Springer Series in Solid State Sciences, Vol. 166; Springer Science & Business Media, 2010.

(50). Hosono H; Kuroki K Iron-based superconductors: Current status of materials and pairing mechanism. Physica C: Superconductivity and its Applications 2015, 514, 399–422.

(51). Shipley AM; Hutcheon MJ; Johnson MS; Needs RJ; Pickard CJ Stability and superconductivity of lanthanum and yttrium decahydrides. Phys. Rev. B 2020, 101, 224511.

(52). Liu H; Naumov II; Hoffmann R; Ashcroft N; Hemley RJ Potential high-Tc superconducting lanthanum and yttrium hydrides at high pressure. Proc. Natl. Acad. Sci. U. S. A. 2017, 114, 6990–6995. [PubMed: 28630301]

(53). Drozdov A; Eremets M; Troyan I; Ksenofontov V; Shylin SI Conventional superconductivity at 203 K at high pressures in the sulfur hydride system. Nature 2015, 525, 73–76. [PubMed: 26280333]

(54). Poole CP; Farach HA; Creswick RJ Superconductivity; Academic Press, 2013.

(55). Shipley AM; Hutcheon MJ; Needs RJ; Pickard CJ High-throughput discovery of high-temperature conventional superconductors. Phys. Rev. B 2021, 104, 054501.

(56). Yuan J; Stanev V; Gao C; Takeuchi I; Jin K Recent advances in high-throughput superconductivity research. Supercond. Sci. Technol. 2019, 32, 123001.

(57). Rodriguez C; Liechtenstein A; Mazin I; Jepsen O; Andersen O; Methfessel M Optical near-zone-center phonons and their interaction with electrons in YBa 2 Cu 3 O 7: results of the local-density approximation. Phys. Rev. B 1990, 42, 2692.

(58). Subedi A; Ortenzi L; Boeri L Electron-phonon superconductivity in A Pt 3 P (A= Sr, Ca, La) compounds: From weak to strong coupling. Phys. Rev. B 2013, 87, 144504.

(59). Duan D; Yu H; Xie H; Cui T Ab initio approach and its impact on superconductivity. Journal of Superconductivity and Novel Magnetism 2019, 32, 53–60.

(60). Kolmogorov A; Shah S; Margine E; Bialon A; Hammerschmidt T; Drautz R New superconducting and semi-conducting Fe-B compounds predicted with an ab initio evolutionary search. Physical review letters 2010, 105, 217003. [PubMed: 21231344]

(61). Gao G; Oganov AR; Li P; Li Z; Wang H; Cui T; Ma Y; Bergara A; Lyakhov AO; Iitaka T; et al. High-pressure crystal structures and superconductivity of Stannane (SnH4). Proc. Natl. Acad. Sci. U. S. A. 2010, 107, 1317–1320. [PubMed: 20080576]

(62). Duan D; Liu Y; Tian F; Li D; Huang X; Zhao Z; Yu H; Liu B; Tian W; Cui T Pressure-induced metallization of dense (H2S) 2H2 with high-Tc superconductivity. Sci. Rep. 2014, 4, 6968. [PubMed: 25382349]

(63). Cooper LN; Feldman D BCS: 50 Years; World Scientific, 2010.

(64). Giustino F Electron-phonon interactions from first principles. Rev. Mod. Phys. 2017, 89, 015003.

(65). Kawamura M; Hizume Y; Ozaki T Benchmark of density functional theory for superconductors in elemental materials. Phys. Rev. B 2020, 101, 134511.

(66). Choudhary K; Garrity KF; Reid AC; DeCost B; Biacchi AJ; Hight Walker AR; Trautt Z; Hattrick-Simpers J; Kusne AG; Centrone A; et al. The joint automated repository for various integrated simulations (JARVIS) for data-driven materials design. npj Comput. Mater. 2020, 6, 173.

(67). Allen PB; Dynes R Transition temperature of strong-coupled superconductors reanalyzed. Phys. Rev. B 1975, 12, 905.

(68). Choudhary K; Zhang Q; Reid AC; Chowdhury S; Van Nguyen N; Trautt Z; Newrock MW; Congo FY; Tavazza F Computational screening of high-performance optoelectronic materials using OptB88vdW and TB-mBJ formalisms. Sci. Data 2018, 5, 180082. [PubMed: 29737975]

(69). Choudhary K; Kalish I; Beams R; Tavazza F High-throughput identification and characterization of two-dimensional materials using density functional theory. Sci. Rep. 2017, 7, 5179. [PubMed: 28701780]

(70). Choudhary K; Bercx M; Jiang J; Pachter R; Lamoen D; Tavazza F Accelerated discovery of efficient solar cell materials using quantum and machine-learning methods. Chem. Mater. 2019, 31, 5900–5908.

(71). Choudhary K; Garrity KF; Ghimire NJ; Anand N; Tavazza F High-throughput search for magnetic topological materials using spin-orbit spillage, machine learning, and experiments. Phys. Rev. B 2021, 103, 155131.

(72). Choudhary K; Garrity KF; Tavazza F High-throughput discovery of topologically non-trivial materials using spin-orbit spillage. Sci. Rep. 2019, 9, 8534. [PubMed: 31189899]

(73). Choudhary K; Garrity KF; Jiang J; Pachter R; Tavazza F Computational search for magnetic and non-magnetic 2D topological materials using unified spin-orbit spillage screening. npj Comput. Mater. 2020, 6, 49.

(74). Choudhary K; Cheon G; Reed E; Tavazza F Elastic properties of bulk and low-dimensional materials using van der Waals density functional. Phys. Rev. B 2018, 98, 014107.

(75). Choudhary K; Garrity KF; Sharma V; Biacchi AJ; Hight Walker AR; Tavazza F High-throughput density functional perturbation theory and machine learning predictions of infrared, piezoelectric, and dielectric responses. npj Comput. Mater. 2020, 6, 64.

(76). Choudhary K; Ansari JN; Mazin II; Sauer KL Density functional theory-based electric field gradient database. Sci. Data 2020, 7, 362. [PubMed: 33087719]

(77). Wines D; Choudhary K; Tavazza F Systematic DFT+U and Quantum Monte Carlo Benchmark of Magnetic Two-Dimensional (2D) CrX3 (X = I, Br, Cl, F). J. Phys. Chem. C 2023, 127, 1176.

(78). Choudhary K; Garrity K Designing high-TC superconductors with BCS-inspired screening, density functional theory, and deep-learning. npj Comput. Mater. 2022, 8, 244.

(79). Choudhary K; Tavazza F Convergence and machine learning predictions of Monkhorst-Pack k-points and plane-wave cut-off in high-throughput DFT calculations. Computational materials science 2019, 161, 300–308.

(80). Bardeen J; Cooper LN; Schrieffer JR Theory of superconductivity. Physical review 1957, 108, 1175.

(81). Anderson OL A simplified method for calculating the Debye temperature from elastic constants. J. Phys. Chem. Solids 1963, 24, 909–917.

(82). Kresse G; Furthmüller, J. Efficient iterative schemes for ab initio total-energy calculations using a plane-wave basis set. Phys. Rev. B 1996, 54, 11169.

(83). Kresse G; Furthmüller, J. Efficiency of ab-initio total energy calculations for metals and semiconductors using a plane-wave basis set. Computational materials science 1996, 6, 15–50.

(84). Klimeš J; Bowler DR; Michaelides A Chemical accuracy for the van der Waals density functional. J. Phys.: Condens. Matter 2010, 22, 022201. [PubMed: 21386245]

(85). Giannozzi P; Baroni S; Bonini N; Calandra M; Car R; Cavazzoni C; Ceresoli D; Chiarotti GL; Cococcioni M; Dabo I; et al. QUANTUM ESPRESSO: a modular and open-source software project for quantum simulations of materials. J. Phys.: Condens. Matter 2009, 21, 395502. [PubMed: 21832390]

(86). Giannozzi P; Baseggio O; Bonfà P; Brunato D; Car R; Carnimeo I; Cavazzoni C; De Gironcoli S; Delugas P; Ferrari Ruffino F; et al. Quantum ESPRESSO toward the exascale. J. Chem. Phys. 2020, 152, 154105. [PubMed: 32321275]

(87). Wierzbowska M; de Gironcoli S; Giannozzi P Origins of low-and high-pressure discontinuities of Tc in niobium. arXiv 2005, arXiv:cond-mat/0504077 (accessed October 1, 2022).

(88). Kawamura M; Gohda Y; Tsuneyuki S Improved tetrahedron method for the Brillouin-zone integration applicable to response functions. Phys. Rev. B 2014, 89, 094515.

(89). Poncé S; Margine ER; Verdi C; Giustino F EPW: Electron–phonon coupling, transport and superconducting properties using maximally localized Wannier functions. Comput. Phys. Commun. 2016, 209, 116–133.

(90). Baroni S; Giannozzi P; Testa A Green's-function approach to linear response in solids. Physical review letters 1987, 58, 1861. [PubMed: 10034557]

(91). Gonze X Perturbation expansion of variational principles at arbitrary order. Phys. Rev. A 1995, 52, 1086. [PubMed: 9912348]

(92). Perdew JP; Ruzsinszky A; Csonka GI; Vydrov OA; Scuseria GE; Constantin LA; Zhou X; Burke K Restoring the density-gradient expansion for exchange in solids and surfaces. Physical review letters 2008, 100, 136406. [PubMed: 18517979]

(93). Garrity KF; Bennett JW; Rabe KM; Vanderbilt D Pseudopotentials for high-throughput DFT calculations. Comput. Mater. Sci. 2014, 81, 446–452.

(94). Lee K-H; Chang K-J; Cohen ML First-principles calculations of the Coulomb pseudopotential μ^*: Application to al. Phys. Rev. B 1995, 52, 1425.

(95). Choudhary K; Tavazza F In 2D Nanoscale Heterostructured Materials; Jit S, Das S, Eds.; Micro and Nano Technologies; Elsevier, 2020; pp 1–11.

(96). Choudhary K; Garrity KF; Tavazza F Data-driven discovery of 3D and 2D thermoelectric materials. J. Phys.: Condens. Matter 2020, 32, 475501. [PubMed: 32590376]

(97). Choudhary K; Tavazza F Predicting anomalous quantum confinement effect in van der Waals materials. Phys. Rev. Mater. 2021, 5, 054602.

(98). Marques M; ders M; Lathiotakis N; Profeta A; Floris M; Fast L; Continenza A; Gross E; Massidda S Ab initio theory of superconductivity. II. Application to elemental metals. Phys. Rev. B 2005, 72, 024546.

(99). Dudarev SL; Botton GA; Savrasov SY; Humphreys CJ; Sutton AP Electron-energy-loss spectra and the structural stability of nickel oxide: An LSDA+U study. Phys. Rev. B 1998, 57, 1505–1509.

(100). Heid R; Bohnen K-P; Sklyadneva IY; Chulkov E Effect of spin-orbit coupling on the electron-phonon interaction of the superconductors Pb and Tl. Phys. Rev. B 2010, 81, 174527.

(101). Gibson G; Meservey R Evidence for spin fluctuations in vanadium from a tunneling study of Fermi-liquid effects. Phys. Rev. B 1989, 40, 8705.

(102). Sankar R; Peramaiyan G; Muthuselvam IP; Butler CJ; Dimitri K; Neupane M; Rao GN; Lin MT; Chou FC Crystal growth of Dirac semimetal ZrSiS with high magnetoresistance and mobility. Sci. Rep. 2017, 7, 40603. [PubMed: 28098209]

(103). Aggarwal L; Singh CK; Aslam M; Singha R; Pariari A; Gayen S; Kabir M; Mandal P; Sheet G Tip-induced superconductivity coexisting with preserved topological properties in line-nodal semimetal ZrSiS. J. Phys.: Condens. Matter 2019, 31, 485707. [PubMed: 31486414]

(104). Ge J-F; Liu Z-L; Liu C; Gao C-L; Qian D; Xue Q-K; Liu Y; Jia J-F Superconductivity above 100 K in single-layer FeSe films on doped SrTiO3. Nat. Mater. 2015, 14, 285–289. [PubMed: 25419814]

(105). Zheng D-D; Gao M; Yan X-W Electron–phonon coupling in heavily electron-doped bulk FeSe: a first-principles investigation. Applied Physics Express 2019, 12, 013003.

(106). Coh S; Cohen ML; Louie SG Large electron–phonon interactions from FeSe phonons in a monolayer. New J. Phys. 2015, 17, 073027.

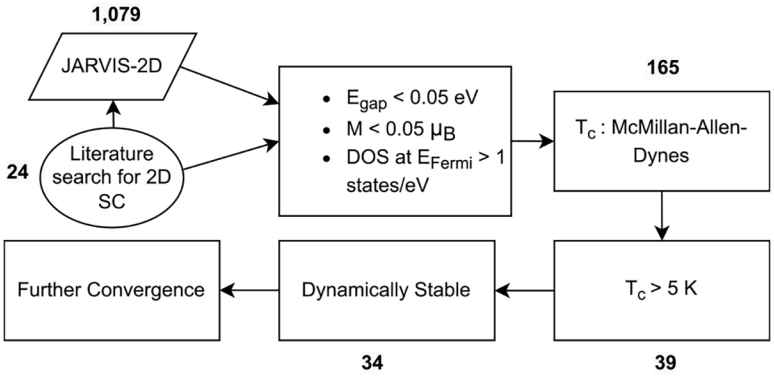

Figure 1.

Full schematic of the high-throughput workflow used to identify high T_C 2D superconductors. The number of materials at each stage of the workflow is given.

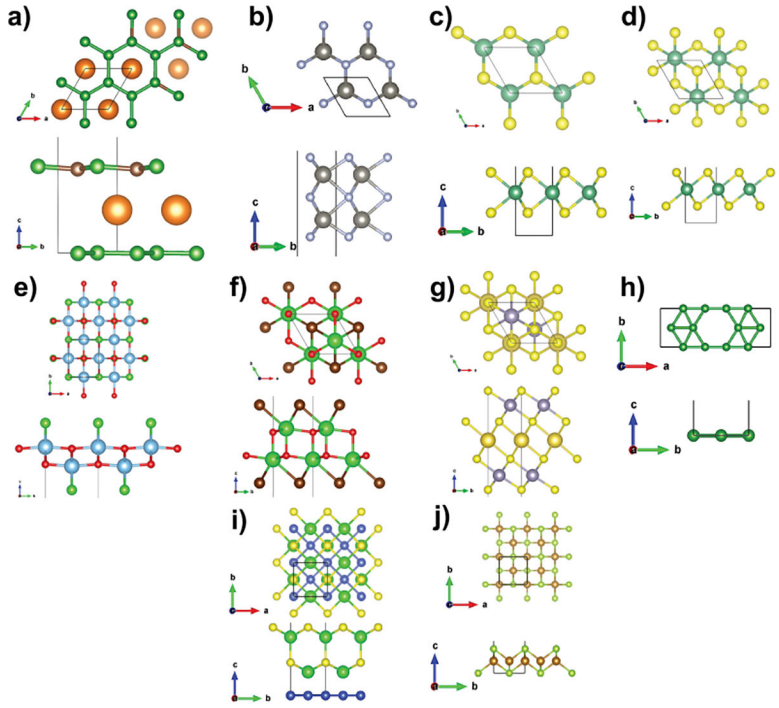

Figure 2.

Top and side views of the atomic structures of candidate 2D superconductors: (a) $Mg_2B_4C_2$, (b) W_2N_3, (c) 2H-NbS_2, (d) 1T-NbS_2, (e) TiClO, (f) ZrBrO, (g) $NaSn_2S_4$, (h) χ-borophene, (i) ZrSiS, and (j) FeSe.

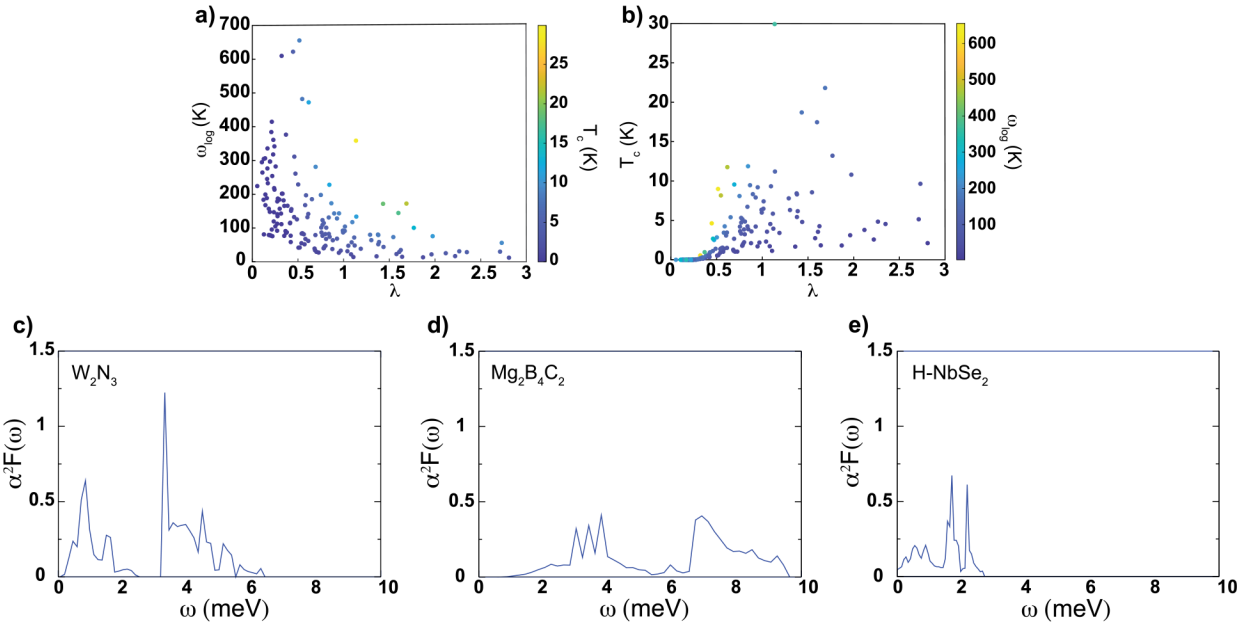

Figure 3.

(a, b) Relation between electron–phonon coupling parameters for all materials and the EPC function of some of the potential candidate superconductors (c) W_2N_3, (d) $Mg_2B_4C_2$, and (e) 2H-$NbSe_2$.

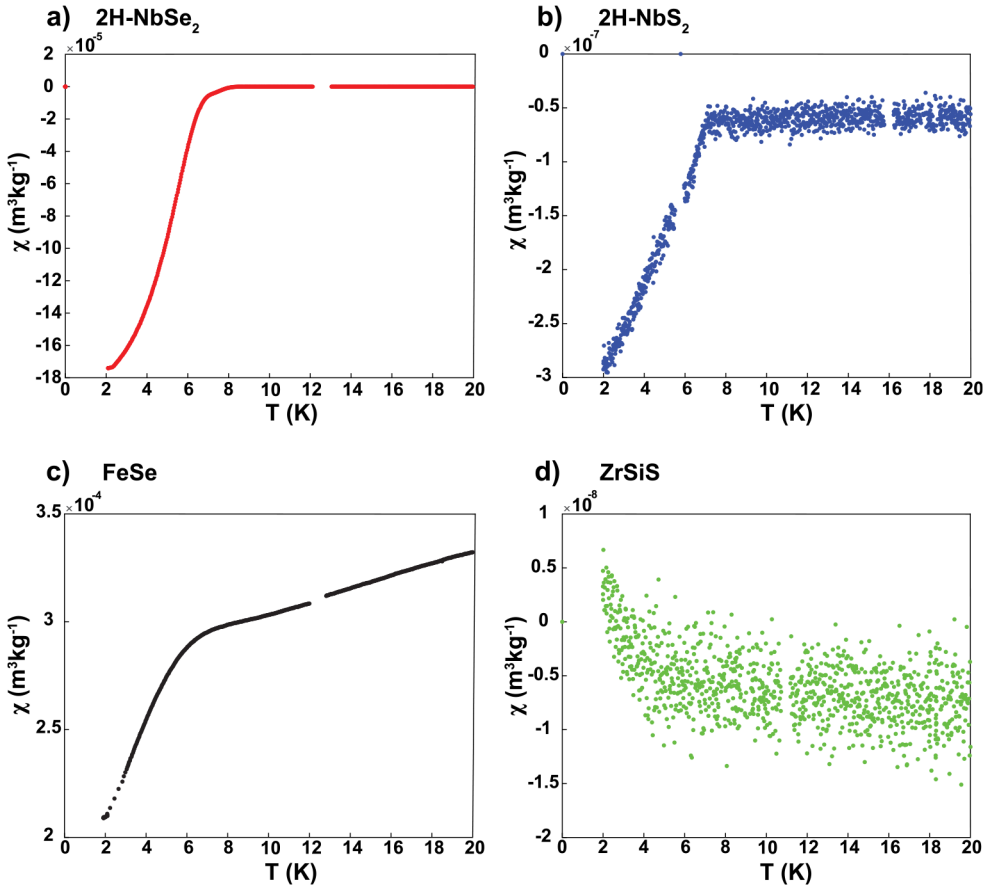

Figure 4.

Experimental zero field-cooled measurements of the DC magnetic susceptibility (using a magnetic field strength of 0.01 T) as a function of temperature in order to determine T_c for layered structures: (a) 2H $NbSe_2$, (b) 2H-NbS_2, (c) FeSe, and (d) ZrSiS.

Table 1.

Results for the 2D Superconductors with a T_c above 5 K[a]

structure	JARVIS ID	λ	ω_{log} (K)	T_c (K)	E_{form} (eV/atom)
$Mg_2B_4N_2$	JVASP-153112	1.7	172.4	21.8	−0.24
w_2n_2	JVASP-153122	1.4	171.7	18.7	0.05
NbO_2	JVASP-31356	1.6	144.5	17.5	−2.25
PtN_2	JVASP-6634	0.8	228.1	11.9	1.59
MgB_2	JVASP-153113	0.6	472.2	11.8	0.44
MoN	JVASP-13586	1.1	133.7	11.2	1.90
TiClO	JVASP-75097	2.7	56.0	9.6	−2.42
B_2N	JVASP-79276	0.7	281.2	9.6	0.09
ZrBrO	JVASP-28185	0.9	173.3	9.5	−2.39
2H-NbS_2	JVASP-646	1.1	117.4	9.3	−1.03
$NaSn_2S_4$	JVASP-6949	0.9	143.4	9.2	−0.60
$Mg_2B_4C_2$	JVASP-153110	0.5	655.5	9.0	−0.28
Nb_2CuS_4	JVASP-75063	1.5	73.1	8.6	−0.52
AuN_2	JVASP-75054	1.4	80.6	8.4	0.76
Nb_2CoS_4	JVASP-27853	0.9	143.2	8.3	−0.59
1T-NbS_2	JVASP-5947	1.4	79.1	8.3	−1.00
χ-Borophene	JVASP-153104	0.5	482.1	8.2	0.48
NbC	JVASP-153115	0.8	197.9	8.1	0.34
ZrSiS	JVASP-153121	0.9	128.2	7.9	−0.77
$CoAs_2$	JVASP-6637	1.3	80.0	7.8	0.25
$\alpha Mg_2B_4N_2$	JVASP-153111	1.0	104.2	7.4	0.06
B_2O	JVASP-153100	4.8	33.3	7.0	−0.73
2H-TaS_2	JVASP-6070	1.0	91.3	6.5	−1.06
2H-$NbSe_2$	JVASP-655	0.9	115.8	6.4	−0.76
$BaSn_4O_8$	JVASP-77697	1.3	64.0	6.3	−1.51
1T-$NbSe_2$	JVASP-5899	3.3	33.6	6.3	−0.74
$LaBi_2O_4$	JVASP-28176	1.4	58.5	6.2	−1.92
BrCY	JVASP-60515	1.0	86.8	6.0	−1.18
2H-$NbTe_2$	JVASP-153106	1.1	71.8	5.8	−0.33
TiSe	JVASP-6010	1.4	51.8	5.4	−0.74
TiS_2	JVASP-774	0.7	185.4	5.4	−1.33
ZrS	JVASP-786	0.8	123.3	5.3	−1.39
$AuSe_2$	JVASP-6601	2.7	29.9	5.1	0.29
VSe	JVASP-77610	0.8	114.7	5.1	−0.47

[a]Values for λ, ω_{log}, T_c, and formation energy per atom are given.